Atomically Sharp Crack Tips in Monolayer MoS_2 and Their Enhanced Toughness by Vacancy Defects

Shanshan Wang[1]†, Zhao Qin[2]†, Gang Seob Jung[2], Francisco J. Martin-Martinez[2], Kristine Zhang[2], Markus J. Buehler[2*], Jamie H. Warner[1*]

[1]Department of Materials, University of Oxford, OX1 3PH, United Kingdom

[2]Department of Civil and Environmental Engineering, MIT, Cambridge MA 02139, USA

Email: jamie.warner@materials.ox.ac.uk; mbuehler@mit.edu;

† These authors contributed equally to this work

Abstract: When a brittle material fractures due to an applied stress, cracks propagate through the material causing mechanical failure. Atomically sharp crack tips at the frontier of crack propagation are predicted but have not been captured experimentally before, which requires both, atomic resolution and crack tracking at much larger length scales. Here, we combine both in-situ aberration-corrected transmission electron microscopy and large-scale molecular dynamics simulations based on a reactive force field to investigate the crack propagation in the monolayer MoS_2 with atomic resolution. We find that brittle fracture in 2D monolayer MoS_2 leads to crack tips with atomic sharpness through the preferential Mo-S bond cleavage along the zigzag lattice direction with least energy release. We show that vacancy defects cause crack deflections, while increasing defect density shifts the fracture mechanism from brittle to ductile by the migration of vacancies in the strain fields and forming a defect network. We demonstrate that adding vacancies to MoS_2 can enhance the fracture toughness of the material by forming defect lines, rendering its crack propagation different from, and leading to even higher fracture toughness, than defected graphene. We show that this mechanism explains the reduced crack propagation speed by adding vacancies as seen in experiments.

One Sentence Summary: In-situ transmission electron microscopy and large-scale atomistic-scale computational simulations with a reactive force field reveal how the interactions between atomically sharp crack tips and defects causes the markedly enhanced fracture toughness by adding vacancies in monolayer MoS_2, along with a comparison to graphene.

Main Text:

Understanding fracture mechanics is critical to avoid mechanical failure in materials and to increase their strength (*1–6*). The basis of fracture in a material is often centered around cracks and their tip fronts as they propagate through the crystal, in a brittle or ductile manner (*7–11*). Brittle fracture is often associated with clean sharp cleavage of bonds that occurs rapidly with fast crack propagation speeds, whilst ductile fracture generally involves some plastic deformation around the tip front that slows down the crack propagation (*12–14*). Preventing a crack from forming brittle propagations can delay mechanical failure and effectively increase the material's fracture toughness. Gaining a deep understanding of this process requires investigation at the atomic level, due to the nature of bond breakage in crack propagation, the nanoscale size of crack tips, interactions with defects and the plasticity generated in ductile materials under

stress. While these atomic behaviors have been theoretically predicted (*15–17*), they have not been revealed before with in-situ experiments with such a detailed description.

Several different imaging techniques have been used to observe cracks in materials, ranging from optical microscopy (microscale) (*18*, *19*), atomic force microscopy (nanoscale) (*20–22*) to transmission electron microscopy (TEM) (atomic scale) (*7*, *10*, *23*). TEM can provide single atom imaging, but in thick bulk materials it is difficult to determine the exact atomic structure of crack tips due to the 2D projection of their 3D structure. This limitation is eliminated in 2D materials, such as graphene, monolayer transition metal dichalcogenides (TMDs) and hexagonal boron nitride (BN) where the atomic positions can be truly interpreted from the 2D projection (*24–26*).

2D materials of different chemistry have very different molecular structures and mechanical properties and it is intriguing how they link to different crack propagation. While fracture in graphene has been heavily investigated (*27–31*), fracture of other 2D materials, such as MoS_2 and BN, is less understood, preventing comparison of their different fracture behavior to understand the essential connection between molecular structure and its fracture mechanism for 2D materials. Classical molecular dynamics (MD) simulation represents a suitable tool to investigate the crack propagation in different 2D materials. It is predicted in MD simulations that defects in graphene can form dislocations and grain boundaries to interact with the crack propagation (*32*, *33*) but there is also evidence that their existence does not strongly alter the crack propagation speed (*34*). However, it is not clear if such mechanism is the same for MoS_2 fracture and how its fracture toughness gets affected by defects.

Here, we examine the structure and dynamics of cracks in suspended single crystals of monolayer MoS_2 and their interaction with vacancy defects at the atomic level using aberration-corrected TEM (AC-TEM). We fully compare our MD simulation based on first-principles based reactive force fields (see its details in SI) against the experimental observations and Density Functional Theory (DFT) calculations and thereafter use simulations to systematically investigate the fracture toughness as a function of vacancy density of MoS_2 and compare to that of graphene. The MoS_2 was grown by chemical vapor deposition and transferred to Si_3N_4 TEM grids with 2 μm holes (figure 1a). Cracks were introduced into MoS_2 in a similar way to prior work on graphene by bombarding the strained 2D membrane with a focused electron beam (e-beam) at 80kV (*31*), figure 1b (video S1). Cracks formed rapidly, preventing their real time imaging, but were stable enough to be captured as a series of quasi-static snapshots. Our MD simulation with the same length scale as experiments, figures 1g and h, shows that mechanically loading an elliptical hole in MoS_2 forms a crack that propagates at the same length scale and with similar geometric features as in those observed in the experiments (figure S1).

Both the experiments and MD simulations show the cracks narrow to an apex tip with atomic sharpness, figures 1c-d and g-i, when containing several atomic step terraces. Long single step terraces show reconstruction at the apex, figures 1e, and f and figures 1i and j (figure S2). The crack propagates by skipping a single Mo-S bond and leaving a flexible chain behind (figure S3). This process is associated with crack deflection, creating step terraces or taking a different propagation direction, which increase the crack path length. Different from graphene, for which cracks occur along both armchair and zigzag lattice directions (*30*), in monolayer MoS_2 cracks predominantly occur along the zigzag lattice direction, associated with cleaving the Mo-S bond, figure 1d.

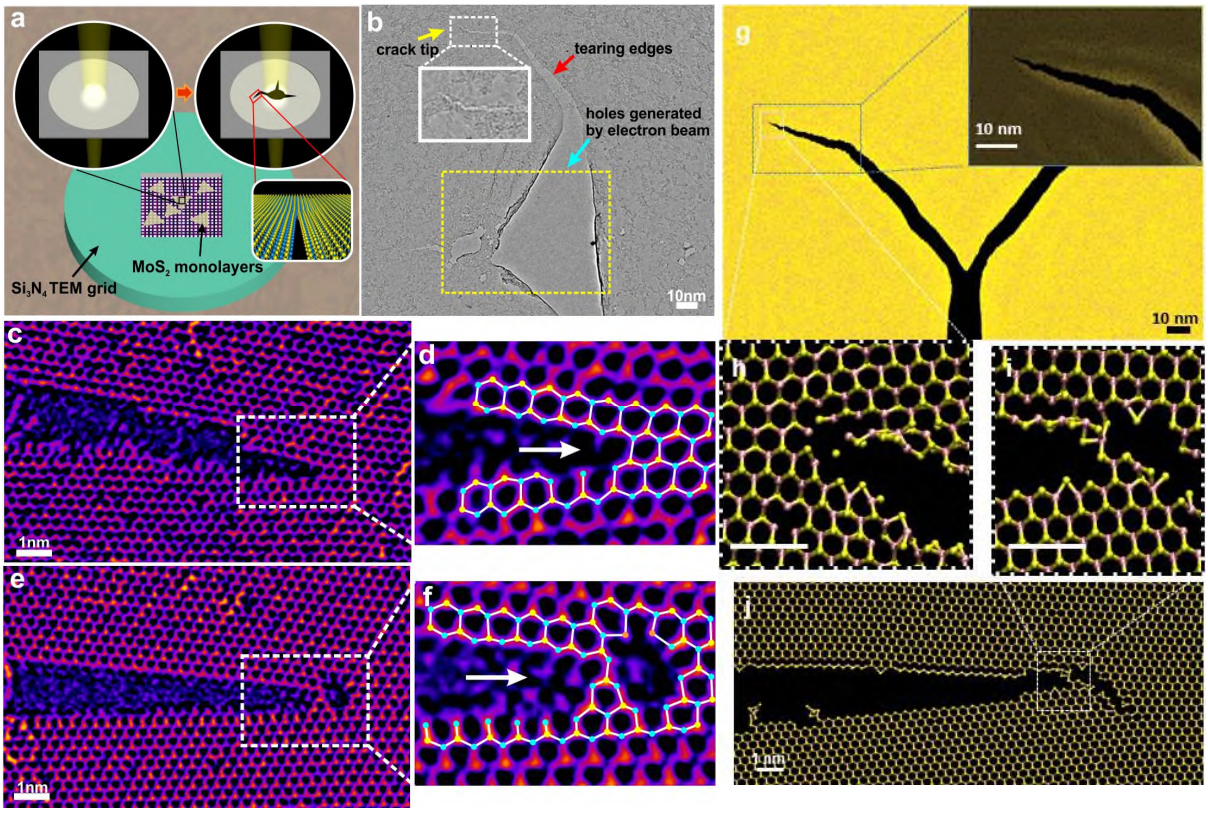

Figure 1. Cracks in a suspended monolayer MoS_2 membrane. (a) Schematic illustration showing transferred CVD-grown triangular-shaped monolayer MoS_2 domains with the size of ~15 μm distributed on the central holey window of the Si_3N_4 TEM grid. Each domain can completely cover several holes. The zoom-in circular window shows the crack generation process by the focused e-beam on the suspended monolayer MoS_2 membrane covered on one TEM hole. (b) TEM image showing the crack microstructure. The crack was developed from a hole created by continuous focused e-beam irradiation, marked by the yellow box. A typical crack propagated along a certain lattice direction can be seen, leaving long and straight teared edges, highlighted by the red arrow. The white dashed box shows the crack morphology in its final propagation stage including the crack tip with a higher magnification image below as an inset. (c-e) High-magnification AC-TEM images showing the atomic structures of different types of cracks around the tip region (panel c and e), with atomic models overlaid (panel d and f) highlighting the detailed configurations of crack tips, labeled by white dashed boxes in panel c and e, respectively. The blue, yellow and orange spheres represent the single Mo atom, double S atoms and the single S atom, respectively. White arrows in (d) and (e) show the direction of further crack propagation. (g-h) A snapshot of MD simulation of the crack propagates from the end of an elliptical hole in a piece of MoS_2 model of 200 by 200 nm^2 under mechanical stretching force. The crack tip shows an atomic sharpness feature. (i-j) A MD simulation snapshot of a different crack propagation by creating a smooth crack edge before creating a step and breaking bonds in front of an intact Mo-S bond, leaving a residue chain behind the crack tip.

Crack propagations in MoS_2 are straight for up to 1μm, forming atomically smooth edges of over nanoscale distances, figures S4a-d. Very tiny (sub-nm) crack deflections are observed across one or two rows of lattice, figure S4a. The cracks have complementary atomic edge terminations, indicative of cleaving the Mo-S bond along the zigzag direction, as shown in figures S4b-d

(figures S5-S7). Occasional 60^o direction changes of the cracks following zigzag orientations are observed, figure S4e, and the near-perfect unzipping along all directions demonstrates brittle fracture. Fracture tests simulations, figure S4f, show that the crack pathway in pristine MoS_2 is sensitive to the initial crack tip orientation, with cracks heading in the zigzag direction having smooth propagation with tiny deflections, figure S4g. A crack heading in the armchair direction propagates with more deflections of 60^o (figures S4e and h), following the zigzag lattice along the initial crack direction. The single layer of Mo and S atoms at the upper right edge are mismatched and lose their connection with the rest of the lattice (figure S8). The computed energy release from sample rupture along the zigzag direction is 2.09±0.13 eV/Å, lower than the armchair direction of 2.48±0.16 eV/Å, agreeing with previous DFT calculations of 2.21 eV/Å for zigzag directions (by considering pair of Mo-S bonds with energy of 7.2 eV and bond distance of 3.25 Å) (figures S4f-i). This explains why cracks predominantly occur along the zigzag direction. The ratio of the energy release is very close to the ratio of the total crack length (cos(30^o)), suggesting that the increment in the crack path length mainly contributes to the delayed crack propagation along the armchair direction.

Exposing the crack tip region to the e-beam causes propagation within a fixed location (figure S9). A fracture speed of ~ 0.2 nm/s, figure 2a to c, is slow enough to capture the dynamics with atomic resolution in AC-TEM. The e-beam introduces S vacancies into the MoS_2 lattice, causing crack path deflections, figures 2d to f. Fast crack propagation in figure S4 occurs in pristine regions of the MoS_2 that are not exposed to the e-beam and have minimal defect density. Simulations with 1% S vacancies under the same loading condition, figures S4f, show different crack propagation compared to pristine MoS_2, figures 2j to m, in agreement with the experimental results. The crack tip can be deflected by defects during propagation and creates step terraces. Deflection occurs at a region between the two S vacancies, and once the crack front passes through the two S vacancies disappear, figure 2e, due to vacancy migration induced by stress concentration around the crack tip. Because of the mobility of vacancies in the stress field, the location of the crack deflection point is not simply determined by the position of static defects, but instead is an evolving dynamic process of vacancy migration and crack propagation by bond unzipping. S vacancies situated away from the crack path, where the stress fields are reduced, remain fixed in their locations as the crack propagates (figures 2d and e), which supports that vacancy migration is induced by stress concentration at the crack tip.

In addition, stress concentrated at the crack tip induces lattice distortions, causing the regularly stacked double S atoms in the (001) crystal orientation to split, figures 2g and h, as well as figures 2j and k (figure S10). However, there is no obvious lattice reconstruction in the tip region. The crack typically propagates by directly unzipping the Mo-S bond (marked by A and B in figure 3h) perpendicular to the tearing path along the zigzag direction. Once the crack tip passes, the distortion in the bonding is reduced, but with some of the S atoms on the S-terminated edge lost or reconstructed to out-of-plane positions. Again, these atomic scale mechanisms are shown in our simulations, inserts of figures 2k-m.

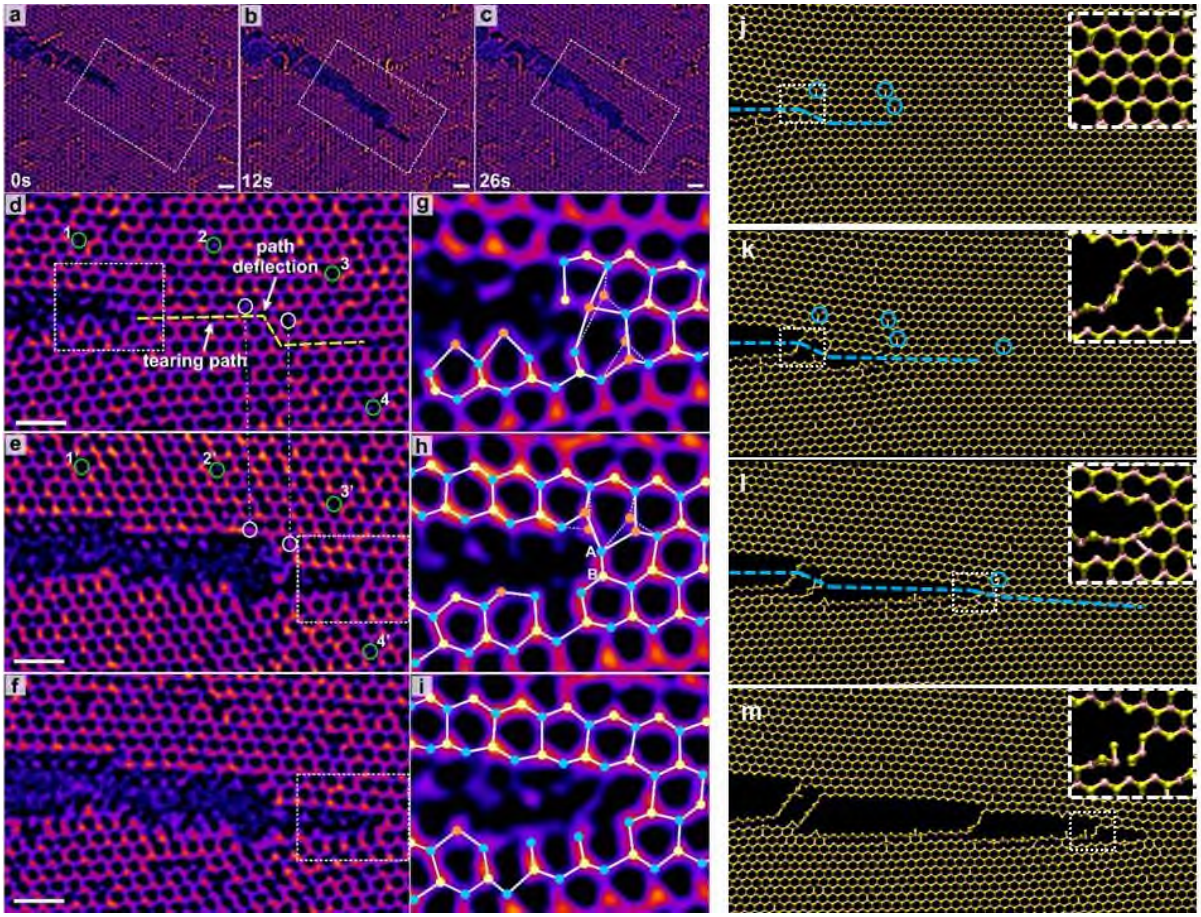

Figure 2. Time series of AC-TEM images showing in-situ dynamics of MoS_2 crack propagation in a mildly defective region. (a-c) A time series of AC-TEM images showing crack movement through a mildly-defective region, having a low concentration of S vacancies. (d-f) AC-TEM images showing the detailed propagation of the crack tip, marked in the region of the white dashed boxes in panel a, b and c, respectively. The white circles in panel d indicate two S vacancies close to the crack path. However, these two vacancies disappeared after the crack tip passing through, as two locations where sitting S vacancies were replaced by regular double stacked S atoms, marked by two white circles in panel e. The yellow dashed line in panel d represents the tearing path of the crack front with a white arrow indicating the path deflection point, situating between two S vacancies. The green circles numbered from 1 to 4 are used to show four S vacancy defects located farther away from the tearing path, compared to those two vacancies marked by white circles. Their locations in panel e are labeled by green circles with corresponding numbers from 1' to 4', respectively. (g-i) AC-TEM images of the crack tip region marked in white boxes in panels d, e and f, respectively, with atomic models overlaid. The blue, yellow and orange circles represent the single Mo atom, double S atoms and the single S atom, respectively. All scale bars are 1 nm. (j-m) Simulation snapshots of the crack propagation in a MoS_2 model with 1% S atom missing, showing the crack pathway is deflected by the defects near the crack tip.

Increasing the vacancy defect concentration in front of a crack tip results in distinctly different crack propagation behavior, with some of the single S vacancies agglomerating into line defects followed by the formation of dislocations and micro-cracks ahead of the tip and small regions of dislocation-free lattice trapped between, figures 3a to e. Simulations show similar dislocation formation when increasing S vacancy density up to 20%, figures 3j to n. The Burgers vector of the dislocation region shows two types, (1,0) dislocation and (1,0) + (0,1) dislocation,

constructed from two |b(1,0)| = 3.1 Å dislocations of (1,0) and (0,1), figures 3f-i (*35*). All these dislocation forms can be identified in the simulation snapshots at the crack tip as shown in figures 3o to r but are not found for fracture test on samples with lower amount of defects. They appear only after the simulation starts, suggesting that they correspond to a more favorable energy state. The dislocations cause blunting of the crack tip, compared to the atomic sharpness found for cracks in regions with low defect density, figures 1 and 2. The continuous creation of dislocations ahead of the crack front decreases the vacancy density in this region (comparing figure 3a with figure 3d and 3e), indicating that the dislocations are partly generated by the aggregation of vacancy defects. Furthermore, large-area dislocation pools are formed by the coalescence of small dislocation cores with dislocation-free micro-crack, figures 3h and 3i. The application of a similar e-beam dose to a MoS_2 region with no cracks only results in vacancies aggregating to form line defects rather than dislocations (figure S11). A fracture velocity of ~0.07 nm/s, in this moderately defective region is the lowest speed measured, compared to the pristine and mildly defective regions. This low value is due to the generation of dislocations and micro-cracks ahead of the crack tips, which might stem from the interaction between the crack front and the increased concentration of point and line defects, disrupting the uniformity of the zigzag lattice plane along which the rapid brittle fracture occurs. This hinders the rapid unzipping of bonds that creates the atomically sharp tips and long-range atomic smoothness of crack edges. This is correlated by increased crack deflection in regions with high defect density, slowing the crack propagation speed (video S2).

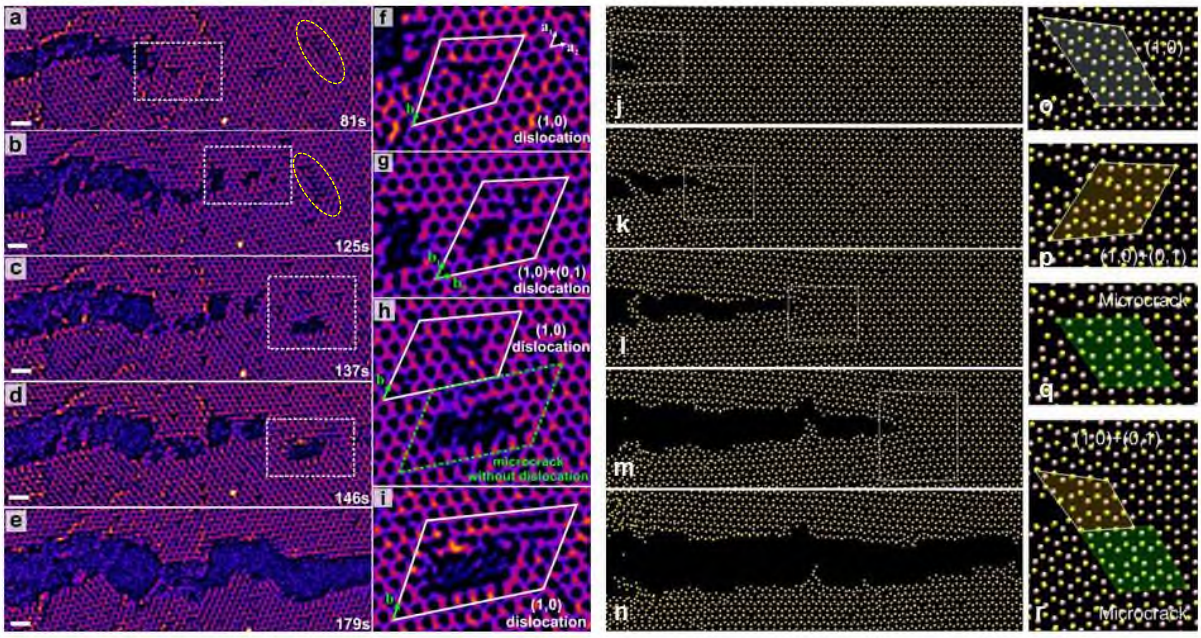

Figure 3. Time series of AC-TEM images showing the in-situ crack propagation within a moderately defective MoS_2 region containing an increased number of vacancy defect. (a-e) A time series of AC-TEM images of crack propagation across an area with a medium concentration of S vacancies, showing the creation of dislocations and micro-cracks ahead of the crack tip marked by white dashed rectangles. The yellow ellipses in panels a and b show the aggregation of some S vacancies into line defects, which subsequently evolve into dislocation pools in panel c as the crack tip approaches. (f-i) AC-TEM images of regions marked in white dashed boxes in panels a to d, respectively. Dislocations with corresponding Burgers' vectors, labeled by green arrows, are shown by drawing Burgers' circuits in white. Dislocation-

free micro-crack is marked by green dashed lines. All scale bars are 1 nm. (j-r) Simulation snapshots of the crack propagation in a MoS_2 model with 20% S atom missing, showing various types of dislocations form at the crack tip. The dislocations interact with the crack propagation by deflecting the crack path and making the crack tip less sharp than material samples with lower defect rates.

In figure 4a we schematically show how the randomly distributed defects aggregate to different forms in MoS_2 and graphene, as S vacancy defects in MoS_2 aggregate to form line defects that are distinctly different to the vacancy aggregates in graphene, for which increasing vacancy density results in dislocation pairs and then finally small holes (figures S12-S17). This schematic is supported by our computational simulations of MoS_2 (figure 4b) and graphene (figure 4c) for comparison, which show that the line defects in MoS_2 helps to guide and deflect the crack in propagation but there is no such mechanism for the small holes and dislocation in graphene. We systematically compute the energy release rate (G_C) and fracture toughness (K_{IC}) of MoS_2 and graphene during mechanical fracture (figures 4d and e) as functions of vacancy density (tables S1 and S2). It is noted that our calculations for graphene fracture agree with previous experimental and simulation results (*33*, *36*). Our results show that MoS_2 has overall higher energy release rate than graphene and initial vacancy increase in MoS_2 causes an increase in fracture toughness, while for graphene adding vacancies only reduces fracture toughness. Surprisingly, the fracture toughness for mildly and moderately defective MoS_2 can exceed that of graphene, figure 4e. This is attributed to the way in which the atomically sharp crack tips interact with the vacancies in MoS_2 compared to graphene.

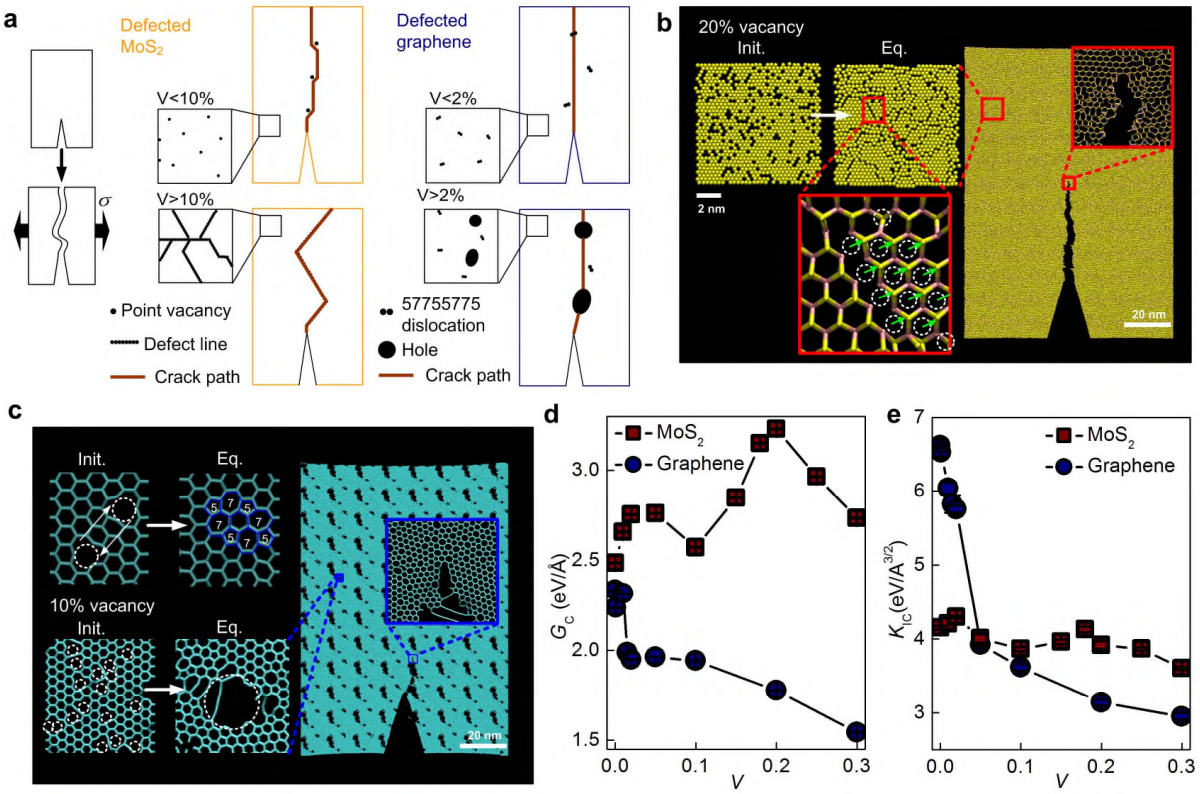

Figure 4. The enhanced fracture toughness of defected MoS_2 and its molecular mechanism. (a) The schematic shows that we apply tensile loading force to material samples on the left and right boundaries until their total failure in our computational simulations. Fracture of defected MoS_2 with different vacancy density (V) is unique as is featured by the deflected crack pathway which is very different from

what is seen in graphene. The crack path associates with the conformation of defects at equilibrium as vacancies in MoS_2 can aggregate and form a defect network composed of lines to guide the crack propagation. (b) The simulation snapshots of a defected MoS_2 sample with initially randomly distributed defects with V=20% before and after equilibration, which shows the merging of vacancies and forming of a defect network. The defect network deflects the crack pathway during fracture. (c) The simulation snapshots of a defected graphene sample with initially randomly distributed defects with V=10% before and after equilibration, while two neighboring vacancies can be healed by forming a 57755775 dislocation, more vacancies form holes instead. The crack pathway in graphene is not significantly deflected. (d-e) The comparison of the energy release rate (G_C, panel d) as the energy release of unit length of the 2D material during fracture and fracture toughness (K_{IC}, panel e) as a function of vacancy density for MoS_2 and graphene, which shows MoS_2 has a higher energy release rate and an superior fracture toughness to graphene once mildly or moderately defected.

In summary, we provide conclusive evidence of the existence of atomically sharp crack tips in 2D materials. An atomically sharp tip means that stress forces are concentrated on the single bond at the apex and therefore propagation can rapidly occur by breaking sequential single bonds along the zig-zag direction. Defects were found to cause crack deflections to form step terraces and redirection. Increasing the density of defects in MoS_2 leads to enhanced fracture toughness, not observed in graphene. Crack tips become blunt and the propagation speed reduces dramatically. Slowing down the crack speed is associated with increased fracture toughness. These results indicate that improved mechanical performance of 2D materials can be achieved by utilizing mildly and moderately defective crystals. This has importance for utilizing 2D materials for designing robust and resilient composites and electronic devices for harsh environments such as space where radiation is extreme and will generate substantial vacancies.

Acknowledgements: SW and JHW acknowledge support from the China Scholarship Council and the Royal Society. ZQ, GSJ, FJMM, KZ and MJB acknowledge support from ONR and AFOSR, and DOD-MURI.

References and Notes

1. J. R. Kermode et al., *Nature* **455**, 1224 (2008).
2. A. Livne, E. Bouchbinder, I. Svetlizky, J. Fineberg, *Science* **327**, 1359 (2010).
3. J. A. Hauch, D. Holland, M. P. Marder, H. L. Swinney, *Phys. Rev. Lett.* **82**, 3823 (1999).
4. T. Cramer, A. Wanner, P. Gumbsch, *Phys. Rev. Lett.* **85**, 788 (2000).
5. K. H. Nam, I. H. Park, S. H. Ko, *Nature* **485**, 221 (2012).
6. D. Wang *et al.*, *Nano Lett.* **7**, 1208 (2007).
7. L. Liu, J. Wang, S. K. Gong, S. X. Mao, *Sci. Rep.* **4**, 4397 (2014).
8. P. Gumbsch, J. Riedle, A. Harnaier, H. F. Fischmeister, *Science* **282**, 1293 (1998).
9. Z. Wu, Y.-W. Zhang, M. H. Jhon, H. Gao, D. J. Srolovitz, *Nano Lett.* **12**, 910 (2012).
10. M. A. L. Marques, H. E. Troiani, M. Miki-Yoshida, M. Jose-Yacaman, A. Rubio, *Nano Lett.* **4**, 811 (2004).
11. S. Hénaux, F. Creuzet, *J. Am. Ceram. Soc.* **83**, 415 (2000).
12. I.-H. Lin, R. Thomson, *Acta Metall.* **34**, 187 (1986).
13. K. M. Flores, R. H. Dauskardt, *Mater. Sci. Eng. A* **319-321**, 511 (2001).
14. F. Cleri, S. Yip, D. Wolf, S. R. Phillpot, *Phys. Rev. Lett.* **79**, 1309 (1997).
15. E. Bitzek, J. R. Kermode, P. Gumbsch, *Int. J. Fract.* **191***, 13 (2015).*
16. M. J. Buehler, A. C. T. van Duin, W. A. Goddard, *Phys. Rev. Lett.* **96**, 095505 (2006).
17. Z. Zhang, A. Kutana, B. I. Yakobson, *Nanoscale* **7**, 2716 (2015).

18. A. Litorowicz, *Cem. Concr. Res.* **36**, 1508 (2006).
19. J. Bisschop, J. G. M. van Mier, *Heron* **44**, 245 (1999).
20. E. Guilloteau, H. Charrue, F. Creuzet, *Europhys. Lett.* **34**, 549 (1996).
21. S. M. Wiederhorn, J.-P. Guin, T. Fett, *Metall. Mater. Trans. A* **42**, 267 (2011).
22. S. Bertolazzi, J. Brivio, A. Kis, *ACS Nano* **5**, 9703 (2011).
23. A. Barreiro, F. Börrnert, M. H. Rümmeli, B. Büchner, L. M. K. Vandersypen, *Nano Lett.* **12**, 1873 (2012).
24. J. H. Warner *et al.*, *Science* **337**, 209 (2012).
25. W. Zhou *et al.*, *Nano Lett.* **13**, 2615 (2013).
26. N. Alem *et al.*, *Phys. Rev. B.* **80**, 155425 (2009).
27. T. Zhang, X. Li, H. Gao, *Int. J. Fract.* (2015).
28. C. Lee, X. Wei, J. W. Kysar, J. Hone, *Science* **321**, 385 (2008).
29. G. López-Polín, J. Gómez-Herrero, C. Gómez-Navarro, *Nano Lett.* **15**, 2050 (2015).
30. K. Kim *et al.*, *Nano Lett.* **12**, 293 (2012).
31. K. Kim *et al.*, *Nat. Commun.* **4**, 2723 (2013).
32. S. S. Terdalkar *et al.*, *Chem. Phys. Lett.* **494**, 218 (2010).
33. G. Jung, Z. Qin, M. J. Buehler, *Extrem. Mech. Lett.* **2**, 52 (2015).
34. R. Jack, D. Sen, M. J. Buehler, *J. Comput. Theor. Nanosci.* **7**, 354 (2010).
35. O. V. Yazyev, S. G. Louie, *Phys. Rev. B* **81**, 195420 (2010).
36. P. Zhang *et al.*, *Nat. Commun.* **5**, 3782 (2014).